Solar Energy Materials & Solar Cells 122 (2014) 287–296

Contents lists available at ScienceDirect

Solar Energy Materials & Solar Cells

journal homepage: www.elsevier.com/locate/solmat

# Solar thermophotovoltaic energy conversion systems with two-dimensional tantalum photonic crystal absorbers and emitters

Youngsuk Nam [a,b,*], Yi Xiang Yeng [a], Andrej Lenert [a], Peter Bermel [a], Ivan Celanovic [a], Marin Soljačić [a], Evelyn N. Wang [a,**]

[a] Massachusetts Institute of Technology, Cambridge, MA 02139, USA
[b] Kyung Hee University, Yongin, South Korea

ARTICLE INFO

*Article history:*
Received 1 July 2013
Received in revised form
3 December 2013
Accepted 6 December 2013

*Keywords:*
Thermophotovoltaic
Solar
Photonic crystals
Tantalum
Emitters
Absorbers

ABSTRACT

Solar thermophotovoltaic (STPV) systems convert solar energy into electricity via thermally radiated photons at tailored wavelengths to increase energy conversion efficiency. In this work, we report the design and analysis of a STPV system with 2D photonic crystals (PhCs) using a high-fidelity thermal-electrical hybrid model that includes the thermal coupling between the absorber/emitter/PV cell and accounts for non-idealities such as temperature gradients and parasitic thermal losses. The desired radiative spectra of the absorber and emitter were achieved by utilizing an optimized two-dimensional periodic square array of cylindrical cavities on a tantalum (Ta) substrate. Various energy loss mechanisms including re-emission at the absorber, low energy emission at the emitter, and a decrease in the emittance due to the angular dependence of PhCs were investigated with varying irradiation flux onto the absorber and resulting operating temperature. The modeling results suggest that the absorber-to-electrical efficiency of a realistic planar STPV consisting of a 2D Ta PhC absorber/emitter and current state of the art InGaAsSb PV cell (whose efficiency is only ~50% of the thermodynamic limit) with a tandem filter can be as high as ~10% at an irradiation flux of ~130 kW/m$^2$ and emitter temperature ~1400 K. The absorber-to-electrical STPV efficiency can be improved up to ~16% by eliminating optical and electrical non-idealities in the PV cell. The high spectral performance of the optimized 2D Ta PhCs allows a compact system design and operation of STPVs at a significantly lower optical concentration level compared with previous STPVs using macro-scale metallic cavity receivers. This work demonstrates the importance of photon engineering for the development of high efficiency STPVs and offers a framework to improve the performance of both PhC absorbers/emitters and overall STPV systems.

© 2013 Elsevier B.V. All rights reserved.

## 1. Introduction

Solar thermophotovoltaic (STPV) systems use an intermediate module that absorbs the solar radiation, and re-radiates photons at high temperatures with tailored wavelengths toward a photovoltaic (PV) cell (Fig. 1). By converting the incident solar radiation to a narrow-band thermal emission matched to the spectral response of the PV cell, STPVs have the potential to overcome the Shockley–Queisser limit for the efficiency of PVs (~33% for 1 sun) [1,2]. STPVs are also highly scalable for a wide range of power capacities, have no moving parts, and allow solar energy storage and the use of an alternative fuel to generate electricity.

Despite the significant potential of STPVs, very few experimental results have reported the system-level efficiency of these systems. Meanwhile, of those reported, the efficiencies were relatively low due to the poor performance of the emitter, absorber, and PV cell and insufficient understanding of the highly coupled energy transport processes among these components. A previous study using an eutectic emitter demonstrated an overall solar-to-electrical efficiency of ~0.025% [3] and a recent experiment with a cylindrical tungsten (W) thermal cavity and germanium (Ge) PV cells demonstrated an overall efficiency of ~0.7% with a high (~3000×) geometrical concentration factor [4]. With a similar cylindrical W cavity layout, ~1% overall efficiency was achieved using gallium antimonide (GaSb) PV cells [5].

One of the biggest challenges in developing high efficiency STPVs is tailoring the spectral response of the absorber and emitter, which operate at high temperatures (>1000 K). Previous studies have investigated various materials including metal-doped MgO, oxides of rare earth materials and tungsten for TPV applications but they have not yet approached the performance of an ideal emitter [6–10]. Recently, the use of photonic crystals (PhCs) with 1D periodic metal/dielectric layers, 2D arrays of cavities and 3D woodpile structures have been suggested to overcome this challenge [9–23]. The PhCs have photonic band structures of propagating and decaying states

* Corresponding authors at: Department of Mechanical Engineering, Kyung Hee University, Yongin, 446-701, Korea. Tel: 82 (31) 201-3652.
** Correspondence to: Department of Mechanical Engineering, Massachusetts Institute of Technology, 77 Massachusetts Avenue, 3-461B, Cambridge, MA 02139, USA. Tel: 1 (617) 324-3311.
*E-mail addresses:* ysnam1@khu.ac.kr (Y. Nam), enwang@mit.edu (E.N. Wang).

0927-0248/$ - see front matter © 2013 Elsevier B.V. All rights reserved.
http://dx.doi.org/10.1016/j.solmat.2013.12.012

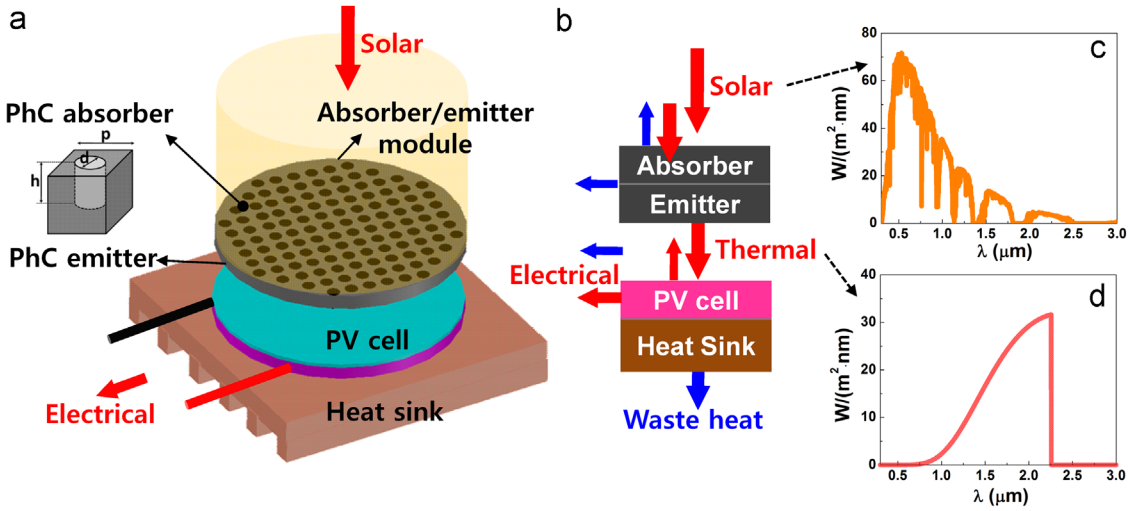


**Fig. 1.** (a) Schematic of a planar STPV consists of PhC absorber and emitter, (b) Energy flow diagram of the STPV that converts solar radiation with a wide spectrum (c) into a tailored spectrum matched to the spectral response of the PV cell (d).

in wavelengths comparable to the length scale of their periodic structures [11,12] and allow narrow-band [13–18] or wide-band thermal emission with sharp, tailored cutoff wavelengths [19–25]. In particular, metallic PhCs with a large band gap and high thermal stability have provided new opportunities in high temperature applications such as STPVs by amplifying absorption and emission within the designed wavelength range while suppressing emission outside [17,19,20,24,26–28]. Long wavelength reflection filters have also been introduced to reflect low energy photons back to the emitter [29–32].

These previous studies with PhCs, however, have focused on component-level rather than system-level performance. Therefore the realistic performance of STPVs and the energy loss mechanisms associated with the integration of these components have not been fully investigated. Furthermore, the spectral performance of the absorber/emitter and system-level thermal losses in STPVs are strongly affected by the operating temperature which is determined by the complex energy transport among the components. Therefore, accurate system-level analysis is critical for the development of high efficiency STPVs.

In this work, we developed a high-fidelity axisymmetric thermal-electrical hybrid system-level model for STPVs with a 2D Ta PhC absorber and emitter. Our model includes radiative and conductive thermal coupling between the absorber, emitter and PV cell, and precisely accounts for non-idealities such as thermal losses through the side wall and the gap between the emitter and PV cell. The emitter/absorber spectra are tailored by varying the dimension of a two-dimensional square array of cylindrical holes created on a Ta substrate. Unlike previous studies, we designed the PhCs through a global optimization process and included the angular dependence of PhCs in the system level analysis. Using our model, we show that ~10% absorber-to-electrical STPV efficiency can be achieved with the developed Ta PhCs and existing PV cells/filters at a relatively low irradiation flux of ~130 kW/m$^2$ and emitter temperature ~1400 K without introducing a complex macro-scale receiver cavity design.

## 2. Energy transport in a STPV

The simplified schematic and energy flow diagram of a planar STPV is shown in Fig. 1. The concentrated solar energy is converted into heat at the absorber and emitted at tailored wavelengths through the emitter that is thermally coupled to the absorber. The thermally radiated high energy photons create electron–hole pairs and generate electricity at the PV cell while low energy photons are wasted as heat. The photons reflected from the PV cell surface or emitted from the cell are re-absorbed on the emitter, or lost to the surrounding.

Due to the multiple energy conversion and transport steps in STPVs, the overall efficiency is determined from the balance between various component-level efficiencies:

$$\eta_{overall} = \frac{H_{abs}\times A_{abs}}{H_c \times A_c}\frac{Q_{abs}}{H_{abs}\times A_{abs}} \times \frac{|Q_{emit}|}{Q_{abs}} \times \frac{|Q_{emit,(E\geq E_g)}|}{|Q_{emit}|} \times \frac{Q_{cell,(E\geq E_g)}}{|Q_{emit,(E\geq E_g)}|} \times \frac{P_{elec,\,max}}{Q_{cell,(E\geq E_g)}}$$
$$= \eta_{collector} \times \eta_{absorber} \times \eta_{adiabatic} \times \eta_{spectral} \times \eta_{cavity} \times \eta_{cell}$$
$$= \eta_{collector} \times \eta_{STPV(abs-elec)}, \quad (1)$$

where $H_c$ and $H_{abs}$ represent the amount of solar irradiation flux onto the collector and absorber surfaces, respectively. The $A_c$ and $A_{abs}$ are the areas of the collector and absorber. $Q_{abs}$, $Q_{emit}$ and $Q_{cell}$ represent the net amount of heat applied to the absorber, emitter and PV cell surfaces, respectively. $P_{elec,max}$ is the maximum power output produced by the PV cell whose band gap is $E_g$.

A certain amount of the solar irradiation onto the absorber is lost due to the reflection, transmission, and the re-emission losses at the absorber, and the ratio between the amount of absorption ($Q_{abs}$) and irradiation ($H_{abs}\times A_{abs}$) is defined as the absorber efficiency $\eta_{absorber} = Q_{abs}/(H_{abs}\times A_{abs})$, where $H_{abs}$ is determined by multiplying the concentration ratio and the solar constant, $H_{abs} = C \times G_s$. The absorbed heat is transferred to the emitter via thermal conduction while losing a certain amount of heat through the side walls. The ratio of the net emission to absorption is defined as the adiabatic efficiency, $\eta_{adiabatic} = |Q_{emit}|/Q_{abs}$. Among the total net thermal emission from the emitter, only high energy ($E \geq E_g$) photons can generate electron–hole pairs in the PV cell, and the ratio of the high energy to the total net emission represents the spectral efficiency $\eta_{spectral} = |Q_{emit,(E\geq E_g)}|/|Q_{emit}|$. Part of the useful emission is lost between the emitter and PV cell, and the ratio of the useful emission arriving at the PV cell surface to the total useful emission defines the cavity efficiency $\eta_{cavity} = Q_{cell,(E\geq E_g)}/|Q_{emit,(E\geq E_g)}|$. Finally, electron–hole recombination, thermalization, and non-ideal optical/electrical performance of the PV cell limit the conversion efficiency and the ratio between the maximum power output to useful emission at the PV cell is defined as the cell efficiency $\eta_{cell} = P_{elec,\,max}/Q_{cell,(E\geq E_g)}$. By multiplying these component level efficiencies, the system-level STPV

efficiency is obtained. We define the absorber-to-electrical STPV efficiency $\eta_{STPV(abs-elec)}$, which excludes the collector loss from the overall efficiency as in Eq. (1) to focus on the effects of the 2D Ta PhC emitter and absorber on the STPV performance.

## 3. Model formulation

We developed a steady-state thermal-electrical hybrid system-level STPV model using the finite element method and an equivalent circuit model. The radiative heat transfer was coupled with conductive and convective heat transfer on each infinitesimal boundary element ($dA$) defined in a 2D axisymmetric framework shown in Fig. 2:

$$-\vec{n}\times(-k\nabla T)=q_{rad}+q_{conv}\quad on\ dA, \tag{2}$$

where $q_{rad}$ and $q_{conv}$ represent the net radiative and convective heat flux applied to the $dA$, respectively. $q_{conv}=h_{conv}(T_{\inf}-T)$ for all of the boundary elements and $q_{rad}$ is defined as $q_{rad,dA_a}$, $q_{rad,dA_e}$ and $q_{rad,dA_s}$ according to the location of the elements (see Fig. 2).

On the absorber (Eq. (3)), the radiative heat flux applied to $dA_a$ ($q_{rad,dA_a}$) was determined from the absorption of incoming solar radiation and re-emission loss:

$$q_{rad,dA_a}=\int_0^\infty \alpha_a(\lambda)H_{dA_a}(\lambda)d\lambda-\int_0^\infty \varepsilon_a(\lambda)\{E_b(\lambda,T_{dA_a})-E_b(\lambda,T_{\inf})\}d\lambda, \tag{3}$$

where $H_{dA_a}(\lambda)$ is the irradiation flux onto $dA_a$ determined by multiplying the standard solar spectrum for concentrated solar applications (AM 1.5D) and the level of optical concentration. $E_b(\lambda,T)$ represents the spectral blackbody emissive power (emitted energy/time/surface area/wavelength) from a surface whose temperature is $T$ and can be expressed as:

$$E_b(\lambda,T)=\frac{2\pi hc^2}{\lambda^5[e^{hc/\lambda k_B T}-1]}, \tag{4}$$

On the emitter (Eq. (5)), the heat flux applied to $dA_e$ was calculated considering the emission loss and the absorption of reflected and direct emission from the PV cell [33]:

$$q_{rad,dA_e}=-\int_0^\infty \varepsilon_e(\lambda)E_b(\lambda,T_{dA_e})d\lambda+\int_0^\infty\int_{A_p}\alpha_e(\lambda)\Big\{\rho_p H_{dA_p}(\lambda)+\varepsilon_p(\lambda)E_b(\lambda,T_{dA_p})\Big\}dF_{dA_e-dA_p}d\lambda, \tag{5}$$

where $H_{dA_p}(\lambda)$ is the irradiation flux onto $dA_p$ (Fig. 2) and $A_p$ is the area of PV cell. The temperature of the PV cell was fixed at 300 K by assuming that the heat generated in the PV cell is dissipated using a thermal management module attached to the backside of the PV cell (see Fig. 1). The view factor, $dF_{dA_e-dA_p}$ quantifies the probability that a photon emitted by the infinitesimal boundary element $dA_e$ of the emitter reaches the element $dA_p$ of the PV cell, which is described as:

$$F_{dA_e-dA_p}=\frac{\cos\theta_e\cos\theta_p}{\pi S^2}dA_p, \tag{6}$$

where $\theta_e$ and $\theta_p$ are the angles between the surface normal vectors and the line connecting $dA_e$ and $dA_p$ of length $S$. Since the absorber/emitter module has a finite thickness, a parasitic radiative loss through the side walls (with emittance $\varepsilon_s$) is defined as:

$$q_{rad,dA_s}=-\int_0^\infty \varepsilon_s(\lambda)\{E_b(\lambda,T_{dA_s})-E_b(\lambda,T_{\inf})\}d\lambda \tag{7}$$

By substituting Eqs. (3)–(7) into Eq. (2) and calculating the energy balance at the entire absorber/emitter module, the temperature distributions at the absorber and emitter were calculated. Then the total photocurrent generated at the PV cell ($I_{ph}$) was determined considering both the direct emission from the emitter and indirect reflections between the emitter and the PV cell:

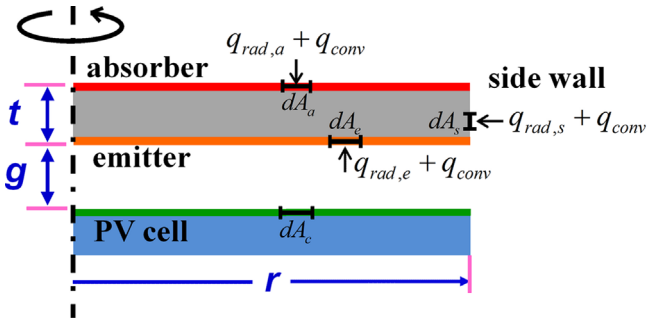


**Fig. 2.** Schematic of the developed 2D axisymmetric finite element model that consists of the absorber/emitter module and PV cell. Heat flux boundary conditions are applied to the infinitesimal boundary elements located on the absorber, emitter and side wall. $r$ and $t$ represent the radius and thickness of a circular absorber/emitter module, respectively, and $g$ represents the spatial gap between the emitter and PV cell.

$$I_{ph}=\int_0^\infty\int_{A_p}\int_{A_e}e\frac{\lambda}{hc}\eta_{ext}(\lambda)\{\varepsilon_e E_b(\lambda,T_e)+\rho_e H_{dAe}(\lambda)\}dF_{dA_p-dA_e}dA_p d\lambda, \tag{8}$$

where $H_{dA_e}(\lambda)$ is the irradiation flux onto $dA_e$ and $\eta_{ext}$ represents the external quantum efficiency of the PV cell. $A_e$ is the area of the emitter. Then the current-voltage (IV) characterization of the PV cell and the maximum electrical power output ($P_{max}$) was obtained from the equivalent circuit model:

$$I=I_{ph}-I_0\left(\exp\left(\frac{e(V+I\,R_s)}{n_i\,k_B T_c}\right)-1\right)-\frac{V+I\,R_s}{R_{sh}}\frac{\partial(IV)}{\partial V}\Big|_{P\ \max}=0\cdot \tag{9}$$

For a realistic prediction, various optical and electrical cell performance parameters such as internal ($\eta_{int}$) and external quantum efficiency ($\eta_{ext}$), reflectance of the cell front surface ($\rho_c$), saturation current ($I_0$), ideality factor ($n_i$), series ($R_s$) and shunt ($R_{sh}$) resistances were determined based on previous experimental characterization [34,35].

## 4. Results and discussion

### 4.1. Ultimate STPV efficiency

Fig. 3 shows the schematic of an ideal STPV operating with an intermediate absorber/emitter module. The ultimate STPV efficiency can be calculated by multiplying the solar-to-thermal efficiency $\eta_{sol-th}$ and the thermal-to-electrical efficiency $\eta_{th-elec}$. Since the theoretical maximum thermal-to-electrical efficiency is equal to the Carnot efficiency operating between two heat reservoirs, the ultimate solar-to-electrical STPV efficiency becomes [2,4]:

$$\eta_{STPV(sol-elec),\ \max}=\eta_{sol-th,\ \max}\cdot\eta_{Carnot}, \tag{10}$$

where $\eta_{Carnot}=(1-T_{\inf}/T_A)$, $T_A$ is the temperature of the intermediate absorber/emitter module and $T_{inf}$ is the surrounding (or PV cell) temperature. The maximum solar-to-thermal efficiency $\eta_{sol-th,\ \max}$ is obtained by assuming a black absorber ($\alpha$ and $\varepsilon$ are equal to 1) and fully concentrated solar irradiation (the solid angles of solar radiation received by the absorber $\Omega_{sun}=\pi$) as follows:

$$\eta_{sol-th,\ \max}=\frac{\sigma T_{sun}^4-\sigma T_A^4}{\sigma T_{sun}^4}=1-\left(\frac{T_A}{T_{sun}}\right)^4\cdot \tag{11}$$

The same maximum solar-to-thermal efficiency can be obtained without the full solar concentration when the solid angle

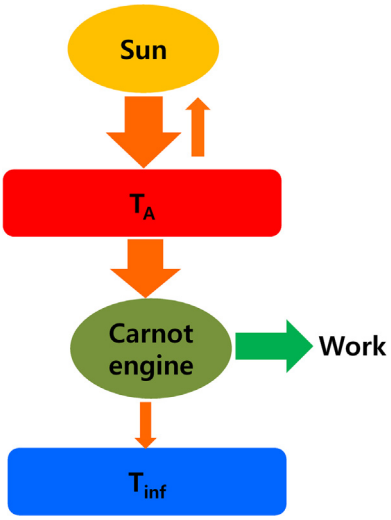


**Fig. 3.** Ideal solar-thermal engine with an intermediate absorber/emitter module.

of the re-emission from the absorber $\Omega_A$ is equal to $\Omega_{sun}$ by introducing a perfect thermal cavity or angular selectivity. From Eqs. (10) and (11), the ultimate solar-to-electrical STPV efficiency becomes:

$$\eta_{STPV(sol-elec),\,\max} = \left\{1-\left(\frac{T_A}{T_{sun}}\right)^4\right\}\left\{1-\left(\frac{T_{inf}}{T_A}\right)\right\}. \quad (12)$$

Eq. (12) shows that the increase in $T_A$ improves the Carnot efficiency but decreases the solar-to-thermal efficiency. The optimal $T_A$ was found to be ~2544 K and the resulting ultimate efficiency was ~85.4% [2,4].

### 4.2. Planar STPVs with cutoff absorbers and emitters

In order to approach the ultimate STPV efficiency described in Eq. (12), we need a monochromatic emitter with a perfect thermal cavity or angular selective absorber. Realizing these absorbers and emitters, however, is challenging with current technology, therefore, we focused on more practical spectrally selective cutoff absorbers and emitters that suppress absorption and emission beyond a cutoff wavelength. The radiative spectra of an ideal cutoff absorber and emitter ($\varepsilon=1$ at $\lambda \le \lambda_{cut}$ and $\varepsilon=0$ at $\lambda > \lambda_{cut}$) is shown in Fig. 4a.

In order to determine the optimal cutoff wavelengths for the emitter and absorber, and to estimate the maximum potential of planar STPVs with cutoff absorber and emitter, we obtained the $\eta_{STPV(abs-elec)}$of planar STPV by varying the cutoff wavelength of emitter $\lambda_{cut,e}$ of the planar STPV (Fig. 4b). The band gap of the PV cell was matched to the $\lambda_{cut,e}$ so that all the emitted photons can create electron–hole pairs in the cell. The cell front surface was assumed to be a blackbody. Various optical and electrical non-idealities of the PV cell except the radiative recombination were neglected [36] and the view factor loss through the gap between the emitter and PV cell was also ignored. For the absorber, the cutoff wavelength $\lambda_{cut,a}$ was determined to maximize the net amount of solar energy absorption by balancing the solar absorption and re-emission loss. The optimal $\lambda_{cut,a}$ and resulting $\eta_{abs}$ obtained by varying optical concentration and absorber temperature are provided in Fig. 4c and Fig. 4d, respectively. In general, the increase in irradiation flux (or optical concentration) and decrease in absorber temperature provide a longer $\lambda_{cut,a}$ (Fig. 4c) and higher $\eta_{abs}$ by reducing the relative portion of re-emission loss compared with solar absorption (Fig. 4d).

Fig. 4b shows that the $\eta_{STPV(abs-elec)}$ of a planar STPV with ideal cutoff absorber, emitter and PV cell can exceed the Shockley–Queisser limit, which agrees with the previous prediction based on the detailed balance theory [37]. We note that the maximum efficiency of planar STPVs with cutoff absorbers and emitters (~42%) is much lower than the ultimate STPV efficiency (~85.4%) calculated from Eq. (12) mainly due to the increase in the re-emission and thermalization losses compared with the ideal configurations assumed in Eqs. (10)–(12).

The desired emitter cutoff wavelength $\lambda_{cut,e}$ (and the band gap of the PV cell) is affected by the amount of parasitic thermal losses through the side walls of the absorber/emitter module (Fig. 4b). Without any parasitic thermal loss through the sidewalls (*i.e.*, effective wall thickness $t_{eff}=\varepsilon_s(t/r)=0$, where $t$ and $r$ represent the thickness and radius of the absorber/emitter module), the optimal $\lambda_{cut,e}$ and band gap are at ~2.07 μm (0.6 eV). When the thermal loss is introduced, the efficiency of STPVs with a shorter $\lambda_{cut,e}$ (larger band gap) decreases more rapidly, because they operate at higher temperatures due to the limited amount of thermal emission. As the result, the optimal $\lambda_{cut,e}$ increases as the $t_{eff}$ increases. For our analysis, the $\lambda_{cut,e}$ was determined to be ~2.25 μm (0.55 eV) since the $t_{eff}$ can be reduced to approximately 0.005 by using a thin substrate with low emissivity (*e.g.*, $t/r=0.05$ and $\varepsilon_s \approx 0.1$). The $\lambda_{cut,e}$ also matches well with the band gap of the existing InGaAsSb PV cells (~0.55 eV) [34,35]. The optimal $\lambda_{cut,a}$ and resulting $\eta_{abs}$ are marked as dashed lines in Fig. 4c and d, respectively, for the planar STPVs whose $\lambda_{cut,e}$ is fixed at 2.25 μm.

### 4.3. Optimized 2D tantalum photonic crystal absorbers and emitters

In order to realize the cutoff absorber and emitter applicable to high temperature systems, we engineered the radiative spectra of emitters and absorbers using a two-dimensional square array of cylindrical holes with period ($p$), diameter ($d$), and depth ($h$) created on a tantalum (Ta) substrate (see Fig. 1 and the inset of Fig. 5). Ta was selected due to its high melting point (3290 K), low vapor pressure and good intrinsic spectral selectivity. It has lower emittance at short wavelengths (1~1.6 μm) than other low emittance materials such as tungsten (W), which enables the tailoring of a wide range of cutoff wavelengths. Ta also has relatively desirable processing properties compared with W [24]. The 2D Ta PhC absorber and emitter exhibit near-blackbody emittance at short wavelengths as well as emittance almost as low as a polished metal at long wavelengths, with a sharp cutoff separating the two regimes. The cutoff wavelength is tunable by adjusting the fundamental cavity resonant frequency through changes in the dimensions of the cavities, while the maximum emittance of the first resonance peak below the cutoff is achieved via Q-matching [21,28].

To calculate the emittance, we utilized the mode matching formalism, whereby emittance is calculated by matching the radiation fields at the boundary of free space and the cylindrical cavities via expansion of the cavity modes [38]. The dispersion of Ta was captured using the Lorentz–Drude model, fit both to the measured reflectance values at room temperature and elevated temperatures [39]. Overall, the normal and hemispherically averaged radiative properties are extremely close to the values obtained from the exact finite-difference time-domain (FDTD) implementation [21,40]. Yet, the mode matching formalism is orders of magnitude faster than the FDTD, which allows easier global optimization of the PhC designs.

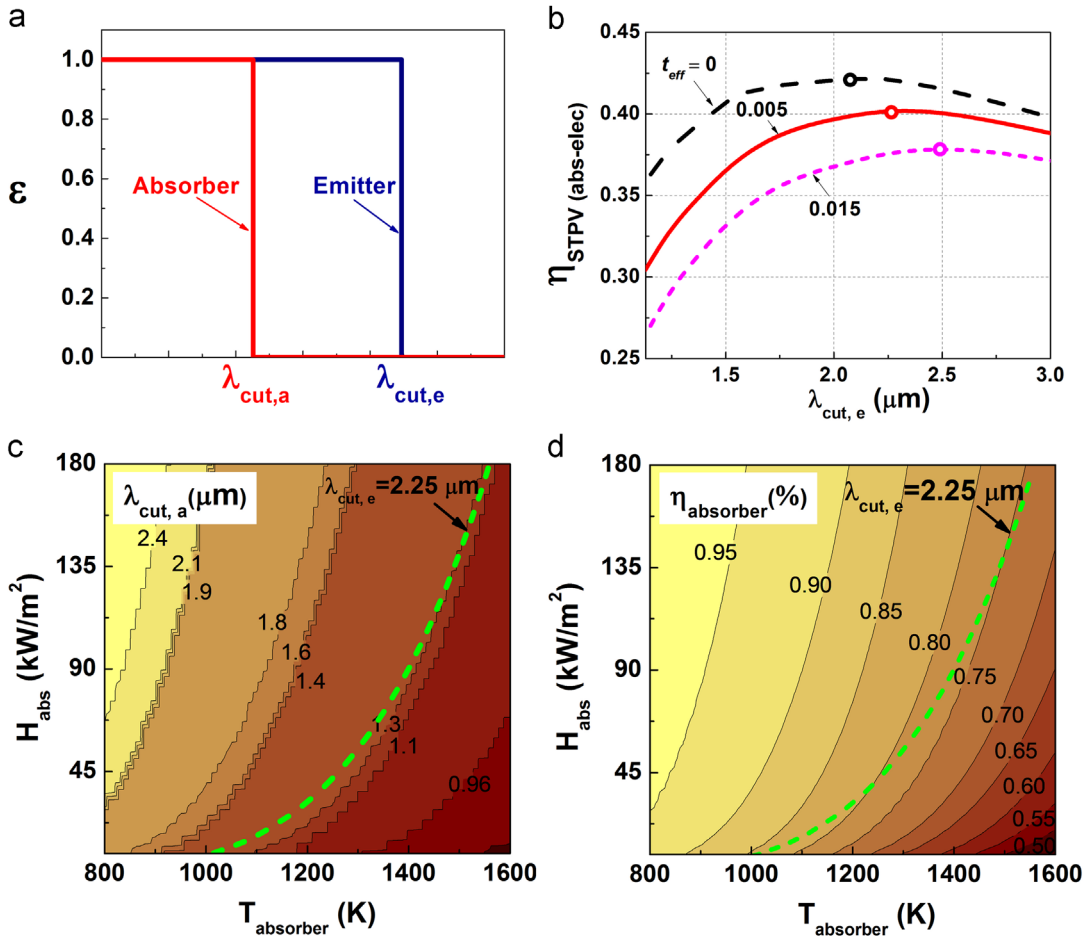


**Fig. 4.** (a) The emittance of the cutoff ideal absorber and emitter, (b) the predicted absorber-to-electrical efficiency of planar STPVs with the ideal cutoff absorber, emitter and PV cell. The effective wall thickness, $t_{eff}=\varepsilon_s(t/r)$, determines the parasitic radiative loss through the side walls, and the dots denote the location of optimal $\lambda_{cut,e}$ providing the maximum overall efficiency, (c) the optimal cutoff wavelength for the absorber $\lambda_{cut,a}$ and (d) the resulting absorber efficiency $\eta_{abs}$ with the ideal cutoff absorbers as a function of irradiation flux onto absorber $H_{abs}$ and absorber temperature $T_{abs}$. Dashed lines in (c) and (d) show the optimal $\lambda_{cut,a}$ and resulting $\eta_{abs}$, respectively, obtained with varying $H_{abs}$ at a fixed $\lambda_{cut,e}=2.25$ μm.

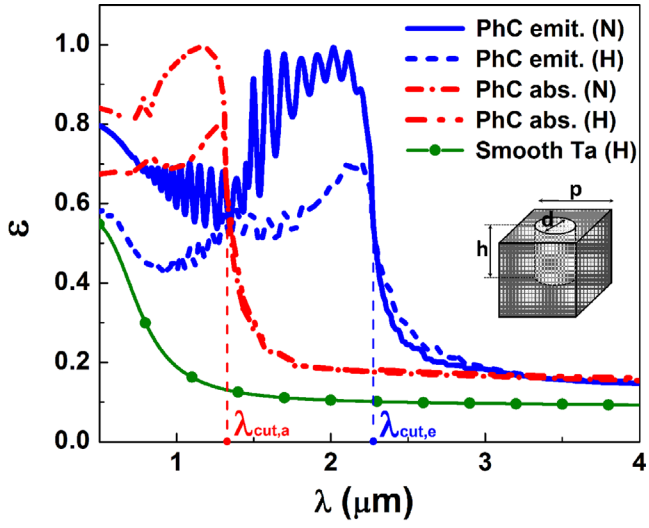


**Fig. 5.** Normal (N) and hemispherically averaged (H) emittance at $T=1200$ K for the developed 2D Ta PhC and smooth Ta absorber/emitter. The cutoff wavelengths of absorber and emitter are tailored to be ~1.3 μm and ~2.3 μm, respectively. The optimal cavity dimensions are determined to be $p=0.68$ μm, $d=0.78$ μm, $h=7.94$ μm for the absorber, and $p=1.24$ μm, $d=1.45$ μm, $h=8.00$ μm for the emitter.

The optimization was performed using both the controlled random search (CRS) algorithm [41] and the multi-level single-linkage (MLSL) algorithm with a low discrepancy sequence (LDS) [42]. The optimization was based on a figure of merit (FOM) measuring how close the performance is compared to an ideal cutoff emitter:

$$FOM = 0.75\overline{E}_{\lambda \le \lambda_{cut}} + 0.25(1-\overline{E}_{\lambda > \lambda_{cut}}), \quad (13)$$

where $\overline{E}_{\lambda \le \lambda_{cut}}$ and $\overline{E}_{\lambda > \lambda_{cut}}$ represent the average emittance above and below the band gap, respectively. Higher weighting was given to increasing emittance below the cutoff wavelength ($\lambda_{cut}$) to ensure high enough power density. Fig. 5 shows the resulting optimized radiative spectra of 2D Ta PhCs and flat Ta obtained at 1200 K. Both normal (N) and hemispherically averaged (H) emittance are provided. The emittance of the 2D PhCs was significantly enhanced for wavelengths shorter than the $\lambda_{cut}$ compared to flat Ta while maintaining the low emissivity at long wavelengths beyond $\lambda_{cut}$. The $\lambda_{cut}$ of the emitter and absorber were tailored to be ~2.25 μm and ~1.3 μm, which takes into account the band gap of the InGaAsSb PV cells (~0.55 eV) and the balance between the solar absorption and re-emission loss, respectively. The optimal cavity dimensions were determined to be $p=0.68$ μm, $d=0.78$ μm, $h=7.94$ μm for the absorber, and $p=1.24$ μm, $d=1.45$ μm, $h=8.00$ μm for the emitter.

Our previous studies have shown that the suggested 2D Ta PhCs can be realized using interference lithography followed by deep reactive ion etching (DRIE) technique [24,28]. Compared with 1D or 3D PhCs consist of multiple interfaces, the 2D metallic PhCs are

more robust and relatively free from thermal stress problems at high ( > 1000 K) operating temperature.

### 4.4. Planar STPVs with the optimized 2D tantalum photonic crystal absorber and emitter

The optimized 2D Ta PhCs were incorporated into the system-level STPV model. To focus on the effect of the 2D Ta PhCs, a simple planar layout composed of a co-axial circular absorber/emitter/PV cell of the same size was investigated (see Figs. 1 and 2). Collimated and uniform incident solar radiation was applied to the absorber while neglecting the collector loss. The normalized thickness ($t/r$) and gap ($g/r$) were fixed at 0.05 for all cases to achieve high ( > 90%) adiabatic and cavity efficiencies. Convective losses and conduction between the emitter and PV cell were neglected by considering a vacuum environment. The irradiation flux onto the absorber was limited to 180 kW/m$^2$ ($\sim$200 suns) to keep the operating temperature below $\sim$1500 K because of the thermal instability of Ta PhCs at very high temperatures [26]. For a realistic prediction, we incorporated existing InGaAsSb PV cells with $\sim$0.55 eV band gap [34,35]. The cell parameters including the spectral quantum efficiencies, reflectance, shunt/series resistance, saturation current and ideality factor were determined from previous experimental characterization [34,35]. A list of the considered STPV configurations is provided in Table 1.

Fig. 6a and b show the system (absorber-to-electrical) and component-level efficiencies of STPVs with the ideal cutoff (*Case I*) and 2D Ta PhC (*Case II-a*) absorber/emitter, respectively. For *Cases I* and *II-a*, the ideal PV cell (0.55 eV) with a blackbody front surface was applied to the model [36]. In all cases, the effects of angular dependence of 2D Ta PhCs were considered by incorporating the hemispherically averaged spectra ('H' in Fig. 5) to the system-level model. Compared with the ideal cutoff emitter (*Case I*), the 2D Ta PhC emitter (*Case II-a*) reduces the spectral efficiency $\eta_{spec}$ over 40% due to the increase in low energy emission beyond $\lambda_{cut,e}$ and decrease in useful emission through the emittance offset below $\lambda_{cut,e}$. (see Fig. 5). The increase in irradiation flux onto the absorber enhances the spectral efficiency since the increase in emitter temperature reduces the wavelength of the emission peak, which decreases the relative portion of the low energy emission. The average temperature of the Ta PhC emitter varies from $\sim$800 K to $\sim$1450 K as the irradiation flux onto the absorber increases from 9 kW/m$^2$ to 180 kW/m$^2$ in Cases *II-a–IV-a* as in Fig. 6c. Due to the uniform irradiation onto the absorber surface, the variation in temperature on the absorber and emitter was negligible. Both adiabatic and cavity efficiencies were maintained around 95% in all cases and not plotted in Fig. 6.

Fig. 6b shows that the 2D Ta PhC absorber (*Case II-a*) also decreases the absorber efficiency $\eta_{abs}$ over 35% compared with the ideal cutoff absorber (*Case I*) due to the increase in the re-emission loss through the emittance offset beyond $\lambda_{cut,a}$. Therefore, STPV efficiency decreases over 60% when the 2D Ta PhCs replace the ideal cutoff absorber and emitter (Fig. 6a). The optimal irradiation flux (or solar concentration) also shifts to a higher level to enhance the operating temperature and reduce the effects of non-ideal emittance offset beyond $\lambda_{cut,e}$. Compared with the ideal PV cell (*Case II-a*), the implementation of the existing InGaAsSb PV cells (*Case III-a* and *IV-a*) drops the cell efficiency $\eta_{cell}$ by 40$\sim$50% due to the optical and electrical non-idealities in the cells. As a result, the absorber-to-electrical efficiency of the STPV composed of the optimized 2D Ta PhC absorber/emitter and the existing InGaAsSb PV cell [34] was predicted to be approximately 8% at an irradiation flux of $\sim$130 kW/m$^2$ and emitter temperature $\sim$1350 K.

### 4.5. Effects of angular dependence of the 2D tantalum photonic crystals

The intrinsic angular selectivity of the designed 2D Ta PhCs arises from the decreasing diffraction threshold as a function of incident polar angle, *i.e.*, a threshold wavelength exactly equal to the periodicity at normal incidence and increasingly larger as the angle of incidence increases. Above the diffraction threshold, the absorptance decreases because there are more channels to reflect back to. Therefore, at larger incident polar angles, the in-band absorption region decreases and has a lower average absorptance, which reduces the hemispherical emittance. A clear distinction between the normal (N) and hemispherically averaged (H) spectra below $\lambda_{cut}$ is shown in Fig. 5.

In Fig. 7a, the effects of the angular dependence on the spectral and absorber efficiencies are investigated by varying the operating temperature of the absorber/emitter and irradiation flux. The decrease in the relative portion of useful emission below $\lambda_{cut}$ due to the angular dependence reduces the spectral efficiency by $\sim$10% throughout the entire considered temperature range. In principle, the angular selectivity of the absorber should have a beneficial effect on the absorber efficiency by suppressing the off-normal re-emission loss without affecting the absorption of collimated solar radiation. In the considered temperature range ( < $\sim$1500 K), however, the benefit is not significant since most of the re-emission from the absorber has relatively long wavelengths beyond $\lambda_{cut}$ that is not affected by the angular dependence. Fig. 7a shows that the angular dependence slightly increased the absorber efficiency over 1400 K but the effect was not significant.

In order to quantify the effect of angular dependence on the STPV efficiency, we incorporated hemispherically averaged (H) spectra into the system-level model where the absorber and emitter are thermally coupled, then compared the results to those obtained with the normal (N) spectra. In the system-level analysis, the decrease in the high energy emission at the emitter not only decreases the spectral efficiency but also increases the operating temperature of the emitter and absorber, which reduces the absorber efficiency by $\sim$5% as shown in Fig. 7b. The changes in other efficiencies including cell, adiabatic, cavity are negligible. As a result, the angular dependence reduced the absorber-to-electrical STPV efficiency $\eta_{STPV(abs-elec)}$ by $\sim$15% compared to the case where the angular dependence is neglected. The analysis suggests that the angular dependence of 2D Ta PhCs needs to be considered for the accurate prediction of performance.

**Table 1**
Simulated planar STPV configurations; normalized thickness ($t/r$) and gap ($g/r$) are fixed at 0.05 for all cases.

| | Absorber | Emitter | Cell front surface | PV cell (0.55 eV) |
|---|---|---|---|---|
| Case I | Ideal cutoff | Ideal cutoff | Blackbody | Thermodynamic limit [36] |
| Case II-a | Ta PhC (Fig. 5) | Ta PhC (Fig. 5) | Blackbody | Thermodynamic limit [36] |
| Case III-a | Ta PhC (Fig. 5) | Ta PhC (Fig. 5) | AR coating | InGaAsSb cell #1 [34] |
| Case IV-a | Ta PhC (Fig. 5) | Ta PhC (Fig. 5) | AR coating | InGaAsSb cell #2 [35] |

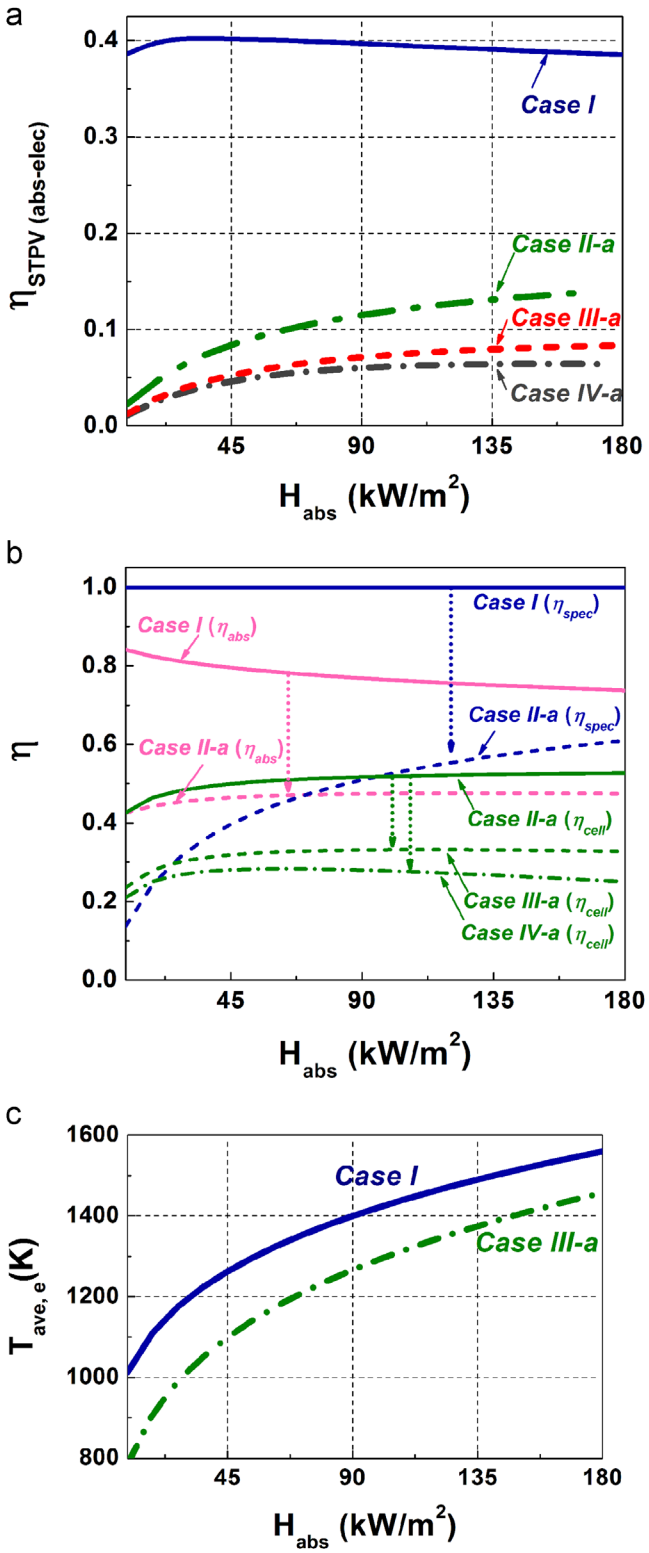


**Fig. 6.** STPV system (absorber-to-electrical) (a) and component level (b) efficiencies for STPVs with various configurations listed in Table 1 (*Cases I*~*Cases IV-a)* and (c) average temperature of the emitter as a function of irradiation flux for *Cases I and III-a*. The emitter temperatures for *Cases II* and *IV* are very similar with *Case III* and not plotted here. In (b), the difference between the cell efficiency of *Cases I* and *II-a* is less than 3% over ~90 kW/m$^2$ of irradiation, therefore, only the value for *Case II-a* is plotted. The presence of non-idealities in the 2D Ta PhCs and PV cell decreases the absorber, emitter and cell efficiencies over 35%, 40% and 40%, respectively, compared with the values obtained with the ideal cutoff absorber, emitter and PV cell (see arrows in (b)). As $H_{abs}$ increases from 9 kW/m$^2$ to 180 kW/m$^2$, the emitter temperature increases approximately from 800 K to 1450 K, which significantly increases the $\eta_{spec}$ and resulting $\eta_{STPV(abs-elec)}$ by reducing the relative portion of low energy emission through the non-ideal emittance offset. The absorber-to-electrical efficiency of the STPV composed of the optimized PhCs and existing InGaAsSb cell (*Case III-a*) is predicted to be ~8% at an irradiation flux of ~130 kW/m$^2$ and emitter temperature ~1350 K.

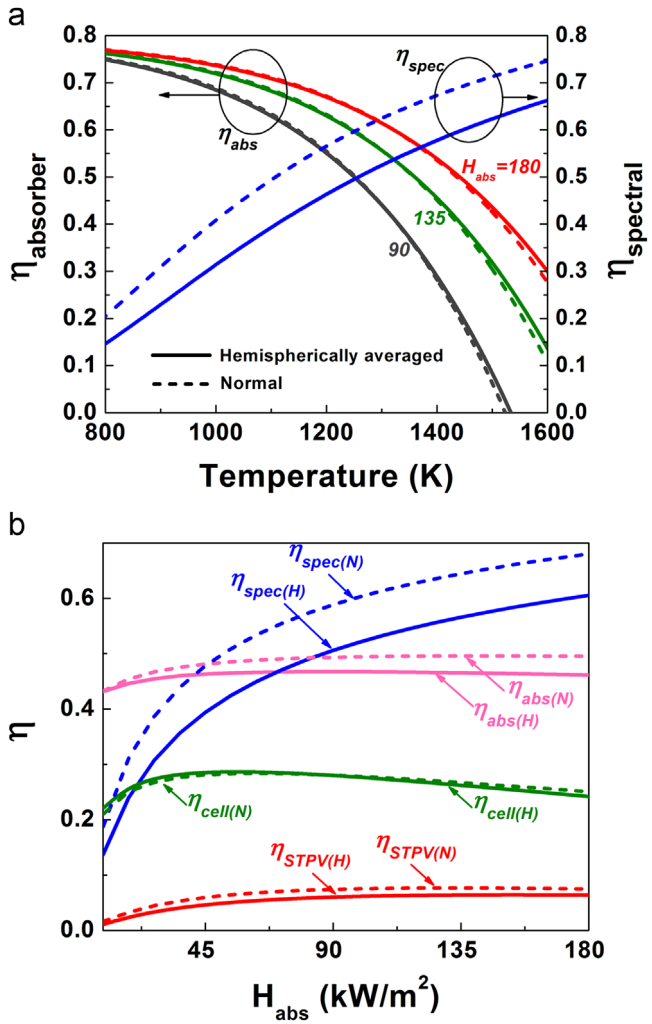


**Fig. 7.** (a) The absorber and emitter efficiencies obtained with normal (N, dashed line) and hemispherically averaged (H, solid line) spectra by varying operating temperature and irradiation flux onto the absorber ($H_{abs}$=90~180 kW/m$^2$). (b) System (absorber-to-electrical) and component-level efficiencies obtained from system-level analysis for STPVs with the 2D Ta PhC absorber/emitter and the existing InGaAsSb cell (*Case III-a*). The angular dependence of the 2D Ta PhCs decreases the absorber, emitter and system efficiencies by approximately 5%, 10% and 15%, respectively, by reducing the useful energy emission below $\lambda_{cut}$ at the emitter and increasing the operating temperature at the absorber.

### 4.6. *Effects of a long wavelength reflection front filter*

Fig. 6a and b show that a significant amount of low energy emission still occurs even with the 2D Ta PhC. To improve the spectral efficiency, we investigated the effects of a long wavelength reflection filter attached to the PV cell on the system-level efficiency. The analysis was based on an existing tandem filter developed by Lockheed Martin whose cutoff wavelength is ~2.4 μm [30,32]. The tandem filter is composed of an interference filter stacked on a InPAs plasma filter, and can be attached onto the front surface of PV cells using an optical adhesive. Table 2 provides a list of considered STPV configurations with the tandem filter.

Fig. 8b shows that the tandem filter (*Case III-b*) indeed improves the spectral efficiency $\eta_{spec}$ over 30% by reflecting the low energy photons back to the emitter. However, the absorber efficiency decreases by ~10% with the filter since the operating temperature increases by ~5% (see the $T_{ave,\ e}$ in Fig. 8a) due to the enhanced re-absorption at the emitter thermally coupled with the absorber. As a result, the use of the tandem front filter enhanced the absorber-to-electrical STPV efficiency by 15~20%, up to approximately 10% at an

**Table 2**
Simulated planar STPV with the long wavelength reflection tandem filter; normalized thickness ($t/r$) and gap ($g/r$) are fixed at 0.05 for all cases.

| | Absorber | Emitter | Cell front surface | PV cell (0.55 eV) |
|---|---|---|---|---|
| Case II-b | Ta PhC (Fig. 5) | Ta PhC (Fig. 5) | Tandem filter [32] | Thermodynamic limit [36] |
| Case III-b | Ta PhC (Fig. 5) | Ta PhC (Fig. 5) | Tandem filter [32] | InGaAsSb cell #1 [34] |
| Case IV-b | Ta PhC (Fig. 5) | Ta PhC (Fig. 5) | Tandem filter [32] | InGaAsSb cell #2 [35] |

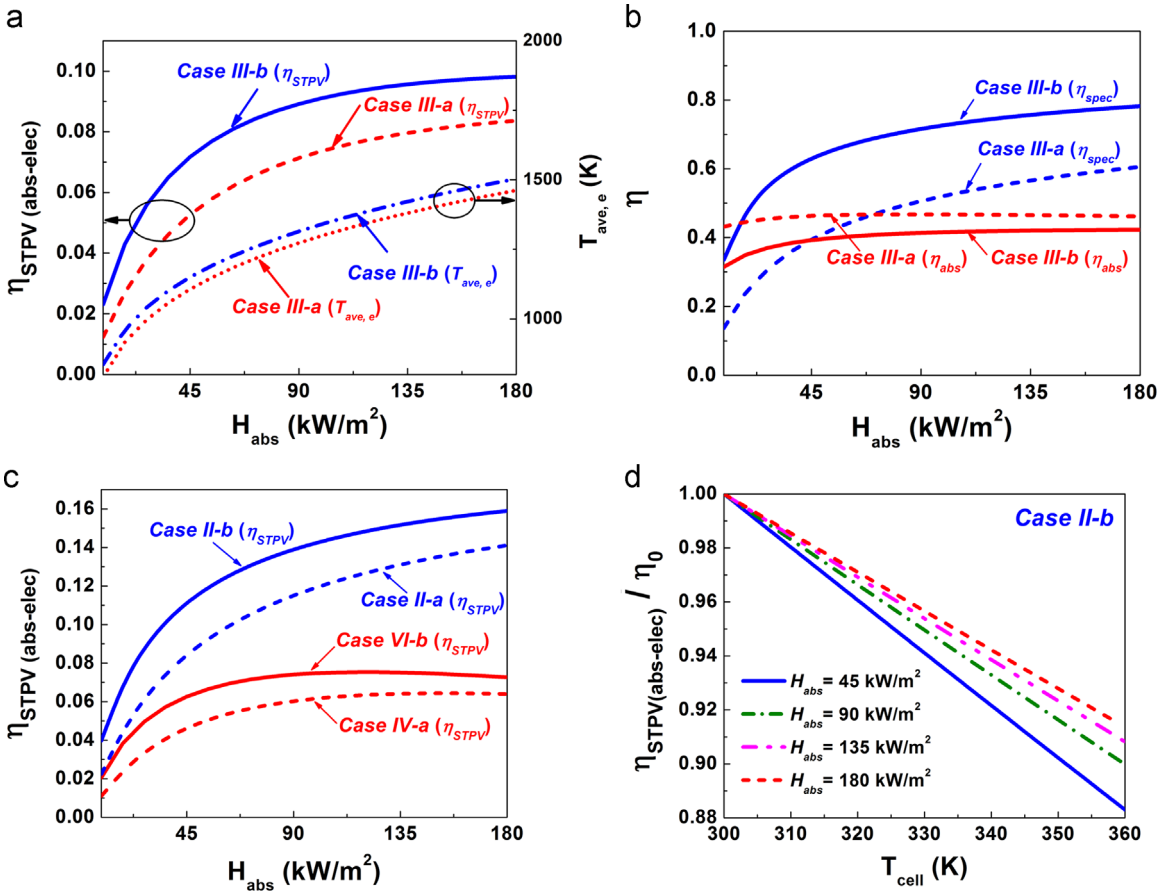


**Fig. 8.** System (absorber-to-electrical) (a) and component-level (b) efficiencies of STPVs with the 2D Ta PhC absorber/emitter and InGaAsSb cell with (*Case III-b*) and without (*Case III-a*) the long wavelength reflection tandem filter at the cell front surface (see Table 2). The average emitter temperature ($T_{ave,e}$) with the filter is also plotted in (a). The emitter temperatures for *Cases II* and *IV* are very similar with *Case III* and not plotted here. The use of the tandem filter improves the spectral efficiency over 30% but reduces the absorber efficiency by ~10% due to the increase in the operating temperature by ~5% as in (a). As a result, the absorber-to-emitter efficiency increases by 15~20%, up to ~10% at an irradiation flux of ~130 kW/m$^2$ and emitter temperature~1400 K (*Case III-b*). (c) The absorber-to-emitter efficiencies with the 2D Ta PhCs and the ideal (*Case II-b*) and another InGaAsSb PV cell (#2, *Case IV-b*). With the ideal PV cell, the absorber-to-electrical STPV efficiency can be improved up to ~16% at an irradiation flux of ~180 kW/m$^2$ and emitter temperature~1500 K. (d) The normalized absorber-to-electrical STPV efficiencies at elevated cell temperatures. The efficiencies were normalized by the values obtained by fixing the cell temperature at 300 K ($\eta_0$).

irradiation flux ~130 kW/m$^2$ and emitter temperature ~1400 K. The overall efficiencies obtained with different cells are shown in Fig. 8c. When the optical and electrical non-idealities in the PV cell increase (*Case IV-b*), the absorber-to-electrical STPV efficiency decreases to ~8%. By eliminating the optical and electrical non-idealities in the cell (*Case II-b*), the absorber-to-electrical STPV efficiency can be improved up to 16% at an irradiation flux of ~180 kW/m$^2$ and emitter temperature~1500 K. Note that it is also important to maintain a low cell temperature to achieve high STPV efficiency. For example, the absorber-to-electrical efficiency of STPV with *Case II-b* configuration decreases by ~10% when the cell temperature increases from 300 K to 360 K (Fig. 6d). In this work, we assumed that the cell temperature was fixed at 300 K since current state-of-the-art thermal management solutions can handle the required heat dissipation requirement. The realistic STPVs with *Case III-b* configurations need to dissipate 2.2~51 kW/m$^2$ heat flux from the cell to maintain the cell temperature constant within the investigated $H_{abs}$ range. The high heat transfer coefficients (on the order of 10–100 kW/m$^2$) obtained from recent single and multi-phase cooling solutions [43,44] can reduce the required temperature difference between the cell and cooling flow and achieve near-constant cell temperature.

A more detailed efficiency breakdown of the STPV composed of the optimized 2D Ta PhCs and the existing InGaAsGb cell with the tandem filter (*Case III-b*) is shown in Fig. 9. The increase in irradiation flux significantly increases the spectral efficiency as the portion of low energy emission decreases due to the increase in the emitter temperature. The system efficiency, however, is not very sensitive to the irradiation flux over ~100 kW/m$^2$ (corresponding to $T_{ave,e} \approx 1300$ K) since the increase in the spectral efficiency is balanced by the decrease in cell efficiency. High

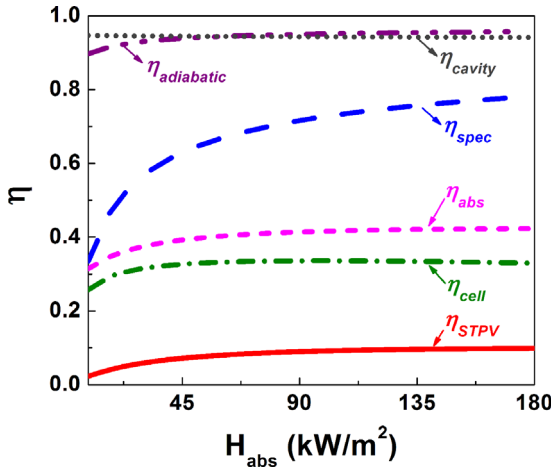


**Fig. 9.** The efficiency breakdown as a function of irradiation flux for the STPV composed of the 2D Ta PhCs and the existing InGaAsSb cell with a tandem filter developed by Lockheed Martin (*Case III-b*). The absorber-to-electrical STPV efficiency is predicted to be ~10% at an irradiation flux of ~130 kW/m$^2$ and emitter temperature ~1400 K. (at 130 kW/m$^2$, $T_{emitter}$=1382.9 K, $\eta_{abs}$=41.9%, $\eta_{spec}$=74.3%, $\eta_{cell}$=33.6%, $\eta_{adiabatic}$=95.3%, $\eta_{cavity}$=94.3%, and $\eta_{STPV(abs\text{-}elec)}$=9.38%).

(~95%) adiabatic and cavity efficiencies are achieved due to the thin ($t/r$=0.05) Ta substrate with low emissivity and small gap ($g/r$=0.05) between the emitter and PV cell. When the $t/r$ and $g/r$ increases by factor of two ($t/r$=$g/r$=0.1), the absorber-to-electrical efficiency decreases by ~3% and ~6% due to the decrease in the adiabatic and cavity efficiency, respectively.

## 5. Conclusions

We present the analysis of a planar STPV composed of 2D Ta PhCs and an existing PV cell/filter using a high-fidelity thermal-electrical hybrid system-level model. By demonstrating the ability to adjust the cutoff wavelength approximately from 1.3 μm to 2.3 μm through changes in geometrical parameters of the cavity, we show that the 2D Ta PhC can be a promising absorber and emitter for STPV applications. The mode matching formalism that is orders of magnitude computationally faster than the FDTD enables us to globally optimize the PhCs, which suggests a valuable strategy for the development of PhCs for various applications. By incorporating the optimized 2D Ta PhC absorber/emitter and current state of the art InGaAsSb PV cell with a tandem filter into our model, we show that the absorber-to-electrical STPV efficiency can be as high as ~10% with a simple planar layout (1:1 emitter-to-absorber area ratio) and a relatively low irradiation flux (~130 kW/m$^2$) and emitter temperature (~1400 K). The absorber-to-electrical STPV efficiency can be improved up to ~16% by eliminating the optical and electrical non-idealities in the PV cell. The efficiency can be further improved by enhancing the spectral performance of PhCs, incorporating multi band gap PV cells and increasing the emitter-to-absorber area ratio with non-planar system designs. The presence of non-ideal emittance offsets in the 2D PhCs decreases the absorber, emitter and overall efficiencies over 35%, 40% and 60%, respectively, compared to the values obtained with the ideal cutoff absorber/emitter. The angular dependence of the 2D PhCs reduces the high energy emission below $\lambda_{cut}$, which leads to a decrease in the overall efficiency by approximately 15% compared to the case in which the angular dependence is neglected. The long wavelength reflection filter attached to the cell front surface improves the spectral efficiency by ~30% but the resulting temperature rise reduces the absorber efficiency by ~10%. This work shows that photon engineering using PhCs can simplify STPV designs by reducing the emitter-to-absorber area ratio and optical concentration factor. Furthermore, our model provides the necessary framework to investigate the energy loss mechanisms in the entire system and improve the overall STPV efficiency.

## Acknowledgments

This material is based upon work supported as part of the MIT S3TEC Center, an Energy Frontier Research Center funded by the U.S. Department of Energy, Office of Science, Office of Basic Energy Sciences under DE-FG02-09ER46577. Y.N. acknowledges the support from Basic Science Research Program through the National Research Foundation of Korea (NRF) funded by the Ministry of Science, ICT & Future Planning (No. 2012R1A1A1014845).

## References

[1] W. Shockley, H.J. Queisser, Detailed balance limit of efficiency of p–n junction solar cells, J. Appl. Phys. 32 (1961) 510–519.
[2] N.-P. Harder, P. Würfel, Theoretical limits of thermophotovoltaic solar energy conversion, Semicond. Sci. Technol. 18 (2003) S151.
[3] H. Yugami, H. Sai, K. Nakamura, N. Nakagawa, H. Ohtsubo. In: Photovoltaic Specialists Conference, 2000. Conference Record of the Twenty-Eighth IEEE, 2000, pp. 1214–1217.
[4] A. Datas, Ph.D. Dissertation, Universidad Politécnica de Madrid, 2011.
[5] V. Khvostikov, S. Sorokina, N. Potapovich, O. Khvostikova, A. Malievskaya, A. Vlasov, M. Shvarts, N. Timoshina, V. Andreev, Thermophotovoltaic generators based on gallium antimonide, Semiconductors 44 (2010) 255–262.
[6] A. Licciulli, D. Diso, G. Torsello, S. Tundo, A. Maffezzoli, M. Lomascolo, M. Mazzer, The challenge of high-performance selective emitters for thermophotovoltaic applications, Semicond. Sci. Technol. 18 (2003) S174.
[7] G.E. Guazzoni, High-temperature spectral emittance of oxides of erbium, samarium, neodymium and Ytterbium, Appl. Spectrosc 26 (1972) 60–65.
[8] L.G. Ferguson, F. Dogan, Spectral analysis of transition metal-doped MgO "matched emitters" for thermophotovoltaic energy conversion, J. Mater. Sci. 37 (2002) 1301–1308.
[9] B. Bitnar, W. Durisch, J.C. Mayor, H. Sigg, H.R. Tschudi, Characterisation of rare earth selective emitters for thermophotovoltaic applications, Sol. Energy Mater. Sol. Cells 73 (2002) 221–234.
[10] M. Ghanashyam Krishna, M. Rajendran, D.R. Pyke, A.K. Bhattacharya, Spectral emissivity of Ytterbium oxide-based materials for application as selective emitters in thermophotovoltaic devices, Sol. Energy Mater. Sol. Cells 59 (1999) 337–348.
[11] E. Yablonovitch, Inhibited spontaneous emission in solid-state physics and electronics, Phys. Rev. Lett. 58 (1987) 2059–2062.
[12] S. John, Strong localization of photons in certain disordered dielectric superlattices, Phys. Rev. Lett. 58 (1987) 2486–2489.
[13] I. Celanovic, D. Perreault, J. Kassakian, Resonant-cavity enhanced thermal emission, Phys. Rev. B: Condens. Matter 72 (2005) 075127.
[14] D.L.C. Chan, I. Celanovic, J.D. Joannopoulos, M. Soljačić, Emulating one-dimensional resonant Q-matching behavior in a two-dimensional system Via Fano resonances, Phys. Rev. A: At. Mol. Opt. Phys. 74 (2006) 064901.
[15] J.-J. Greffet, R. Carminati, K. Joulain, J.-P. Mulet, S. Mainguy, Y. Chen, Coherent emission of light by thermal sources, Nature 416 (2002) 61–64.
[16] M.U. Pralle, N. Moelders, M.P. McNeal, I. Puscasu, A.C. Greenwald, J.T. Daly, E.A. Johnson, T. George, D.S. Choi, I. El-Kady, R. Biswas, Photonic crystal enhanced narrow-band infrared emitters, Appl. Phys. Lett. 81 (2002) 4685–4687.
[17] S.L. J Fleming, I. El-Kady, R. Biswas, K. Ho, All-metallic three-dimensional photonic crystals with a large infrared bandgap, Nature 417 (2002) 52.
[18] V. Mizeikis, K.K. Seet, S. Juodkazis, H. Misawa, Three-dimensional Woodpile photonic crystal templates for the infrared spectral range, Opt. Lett. 29 (2004) 2061–2063.
[19] P. Bermel, M. Ghebrebrhan, W. Chan, Y.X. Yeng, M. Araghchini, R. Hamam, C.H. Marton, K.F. Jensen, M. Solja?i, J.D. Joannopoulos, S.G. Johnson, I. Celanovic, Design and global optimization of high-efficiency thermophotovoltaic systems, Opt. Express 18 (2010) A314–A334.
[20] I. Celanovic, N. Jovanovic, J. Kassakian, Two-Dimensional Tungsten Photonic, Crystals as selective thermal emitters, Appl. Phys. Lett. 92 (2008) 193101–193103.
[21] M. Ghebrebrhan, P. Bermel, Y.X. Yeng, I. Celanovic, M. Soljačić, J.D. Joannopoulos, Tailoring thermal emission Via Q matching of photonic crystal resonances, Phys. Rev. A: At. Mol. Opt. Phys. 83 (2011) 033810.
[22] E. Rephaeli, S. Fan, Absorber and emitter for solar thermo-photovoltaic systems to achieve efficiency exceeding the Shockley-Queisser limit, Opt. Express 17 (2009) 15145–15159.

[23] N.P. Sergeant, O. Pincon, M. Agrawal, P. Peumans, Design of wide-angle solar-selective absorbers using aperiodic metal-dielectric stacks, Opt. Express 17 (2009) 22800–22812.
[24] S.N. Veronika Rinnerbauer, Yi Xiang Yeng, Walker R. Chan, Jay J. Senkevich, John D. Joannopoulos, Marin Soljačić and Ivan Celanovic Recent Developments in High-temperature Photonic Crystals for Energy Conversion, Energy Environ. Sci. 5 (2012) 8815–8823.
[25] C. Wu, B.N. III, J. John, A. Milder, B. Zollars, S. Savoy, G. Shvets, Metamaterial-based integrated plasmonic absorber/emitter for solar thermo-photovoltaic systems, J. Opt. 14 (2012) 024005.
[26] K.A. Arpin, M.D. Losego, P.V. Braun, Electrodeposited 3d tungsten photonic crystals with enhanced thermal stability, Chem. Mater. s 23 (2011) 4783–4788.
[27] E.R. Brown, O.B. McMahon, Large electromagnetic stop bands in metallodi-electric photonic crystals, Appl. Phys. Lett. 67 (1995) 2138–2140.
[28] Y.X. Yeng, M. Ghebrebrhan, P. Bermel, W.R. Chan, J.D. Joannopoulos, M. Soljačić, I. Celanovic, Enabling high-temperature nanophotonics for energy applications, Proc. Nat. Acad. Sci. 109 (2012) 2280–2285.
[29] J. TD Rahmlow, D. DePoy, P. Fourspring, H. Ehsani, J. Lazo-Wasem, E. Gratiix, In: AIP Conference Proceedings., 2007, pp. 59.
[30] R.T. Kristensen, J.F. Beausang, D.M. DePoy, Frequency selective surfaces as near-infrared electromagnetic filters for thermophotovoltaic spectral control, J. Appl. Phys. 95 (2004) 4845–4851.
[31] S.I. Mostafa, N.H. Rafat, S.A. El-Naggar, One-dimensional metallic-dielectric (Ag/Sio2) photonic crystals filter for thermophotovoltaic applications, Renewable Energy 45 (2012) 245–250.
[32] E. Brown, P. Baldasaro, S. Burger, L. Danielson, D. DePoy, J. Dolatowski, P. Fourspring, G. Nichols, W. Topper, T. Rahmlow, The Status of Thermophotovoltaic Energy Conversion Technology at Lockheed Martin Corporation, LM-04K068, 2004.
[33] E.M. Sparrow, A. Haji-Sheikh, A generalized variational method for calculating radiant interchange between surfaces, J. Heat Transfer 87 (1965) 103–109.
[34] W.D. Michael, F.B. John, E. Hassan, G.J. Nichols, M.D. David, R.D. Lee, T. Phil, D.R. Kevin, J.B. Edward, R.B. Steven, M.F. Patrick, F.T. William, P.F. Baldasaro, A.W. Christine, K.H. Robin, K.C. Michael, W.T. George, A.S. Zane, T. Gordon, L. Jizhong, M. Ramon, D. Dmitry, A. Sergei, L.B. Gregory, L. Serge, Quaternary Ingaassb thermophotovoltaic diodes, electron devices, IEEE Trans. 53 (2006) 2879–2891.
[35] W. Chan, R. Huang, C. Wang, J. Kassakian, J. Joannopoulos, I. Celanovic, Modeling low-bandgap thermophotovoltaic diodes for high-efficiency portable power generators, Sol. Energy Mater. Sol. Cells 94 (2010) 509–514.
[36] P. Baruch, A. De Vos, P.T. Landsberg, J.E. Parrott, On some thermodynamic aspects of photovoltaic solar energy conversion, Sol. Energy Mater. Sol. Cells 36 (1995) 201–222.
[37] A. Datas, C. Algora, Detailed balance analysis of solar thermophotovoltaic systems made up of single junction photovoltaic cells and broadband thermal emitters, Sol. Energy Mater. Sol. Cells 94 (2010) 2137–2147.
[38] J. Bravo-Abad, F.J. García-Vidal, L. Martín-Moreno, Resonant transmission of light through finite chains of subwavelength holes in a metallic film, Phys. Rev. Lett. 93 (2004) 227401.
[39] Y.S. Touloukian, D.P. DeWitt, Thermal Radiative Properties: Metallic Elements and Alloys, IFI/Plenum, New York, 1970.
[40] A.F. Oskooi, D. Roundy, M. Ibanescu, P. Bermel, J.D. Joannopoulos, S.G. Johnson, Meep: a flexible free-software package for electromagnetic simulations by the Fdtd method, Comput. Phys. Commun. 181 (2010) 687–702.
[41] W.L. Price, Global optimization by controlled random search, J. Optim. Theory Appl. 40 (1983) 333–348.
[42] S. Kucherenko, Y. Sytsko, Application of deterministic low-discrepancy sequences in global optimization, Comput. Optim. Appl. 30 (2005) 297–318.
[43] G.S. Hwang, Y. Nam, E. Fleming, P. Dussinger, Y.S. Ju, M. Kaviany, Experiment, International Journal of Heat and Mass Transfer, Multi-Artery Heat Pipe Spreader (2010) 2662–2669.
[44] P.-S. Lee, S.V. Garimella, D. Liu, Investigation of heat transfer in rectangular microchannels, Int. J. Heat Mass Transfer 48 (2005) 1688–1704.